



# **Geophysical Research Letters**\*



# **RESEARCH LETTER**

10.1029/2023GL105134

#### **Key Points:**

- A global survey of electron precipitation is performed using the pitch angle and energy resolved data from Electron Losses and Fields INvestigation CubeSats
- At ~1 MeV, electron precipitation is strongest at L > ~6 near midnight and is enhanced near dusk during active times
- The energy spectrum of the precipitation ratio shows reversal points indicating energy dispersion in L shells in the slot region and L > ~6

#### **Supporting Information:**

Supporting Information may be found in the online version of this article.

#### Correspondence to:

M. Qin and W. Li, mqin1@bu.edu; wenli77@bu.edu

#### Citation:

Qin, M., Li, W., Shen, X.-C., Angelopoulos, V., Selesnick, R., Capannolo, L., et al. (2024). Global survey of energetic electron precipitation at low Earth orbit observed by ELFIN. *Geophysical Research Letters*, 51, e2023GL105134. https://doi. org/10.1029/2023GL105134

Received 30 JUN 2023 Accepted 10 NOV 2023

© 2024. The Authors.

This is an open access article under the terms of the Creative Commons Attribution-NonCommercial-NoDerivs License, which permits use and distribution in any medium, provided the original work is properly cited, the use is non-commercial and no modifications or adaptations are made.

# Global Survey of Energetic Electron Precipitation at Low Earth Orbit Observed by ELFIN

Murong Qin<sup>1</sup>, Wen Li<sup>1</sup>, Xiao-Chen Shen<sup>1</sup>, Vassilis Angelopoulos<sup>2</sup>, Richard Selesnick<sup>3</sup>, Luisa Capannolo<sup>1</sup>, Qianli Ma<sup>1,4</sup>, Anton Artemyev<sup>2</sup>, and Xiao-Jia Zhang<sup>2,5</sup>

<sup>1</sup>Center for Space Physics, Boston University, Boston, MA, USA, <sup>2</sup>Department of Earth, Planetary, and Space Sciences, University of California, Los Angeles, CA, USA, <sup>3</sup>Space Vehicles Directorate, Air Force Research Laboratory, Kirtland AFB, NM, USA, <sup>4</sup>Department of Atmospheric and Oceanic Sciences, University of California, Los Angeles, CA, USA, <sup>5</sup>Department of Physics, The University of Texas at Dallas, Richardson, TX, USA

**Abstract** We statistically evaluate the global distribution and energy spectrum of electron precipitation at low-Earth-orbit, using unprecedented pitch-angle and energy resolved data from the Electron Losses and Fields INvestigation CubeSats. Our statistical results indicate that during active conditions, the  $\sim$ 63 keV electron precipitation ratio peaks at L > 6 at midnight, whereas the spatial distribution of precipitating energy flux peaks between the dawn and noon sectors.  $\sim$ 1 MeV electron precipitation ratio peaks near midnight at  $L > \sim$ 6 but is enhanced near dusk during active times. The energy spectrum of the precipitation ratio shows reversal points indicating energy dispersion as a function of L shell in both the slot region and at  $L > \sim$ 6, consistent with hiss-driven precipitation and current sheet scattering, respectively. Our findings provide accurate quantification of electron precipitation at various energies in a broad region of the Earth's magnetosphere, which is critical for magnetosphere-ionosphere coupling.

Plain Language Summary Precipitation into the Earth's upper atmosphere is an important loss process of radiation belt electrons and can change the ionospheric conductance and atmospheric chemistry. Electrons can be moved into the loss cone through either wave-particle interactions or due to special magnetic field geometries, such as current sheet scattering (CSS). To determine the relative contribution of wave-particle interactions and CSS, it is crucial to investigate the global distribution and energy spectra of the electron precipitation rate. Previous measurements of energetic electron precipitation at low-Earth-orbit either had low resolution in pitch angle and energy or were contaminated by ions and penetrating particles. In this study, we used data from the twin Electron Losses and Fields INvestigation CubeSats, which do not suffer from similar deficiencies, to statistically analyze the dependence of energetic electron precipitation rates on geomagnetic activity, with high resolution in both pitch angle and energy. These findings cast new light on the physical mechanisms that determine the precipitation rate from the magnetosphere into the atmosphere and may have implications for future studies of the ionospheric conductivity and atmospheric chemistry.

## 1. Introduction

Energetic electron ( $>\sim$ 10 s keV) precipitation can be driven by various processes, such as pitch angle scattering by plasma waves including whistler-mode chorus waves, hiss waves and electromagnetic ion cyclotron (EMIC) waves (e.g., Li & Hudson, 2019; Millan & Thorne, 2007; Ripoll et al., 2020; Thorne, 2010), or by specific magnetic field geometries, such as current sheet scattering (CSS) (Smith et al., 2016; Yahnin et al., 2016). Chorus waves are typically observed with peak intensity at L < 8 on the nightside and  $L \sim 7$ –9 in the prenoon sector (Li et al., 2009, 2011; Meredith et al., 2012). Dayside chorus waves are less dependent on geomagnetic activity and occur over a wider range of magnetic latitudes ( $\pm 30^{\circ}$ ) along the magnetic field lines than nightside chorus waves (Li et al., 2009; Meredith et al., 2012). Chorus waves can drive energetic electron precipitation to produce diffuse aurora (Ma et al., 2020; Thorne et al., 2010), pulsating aurora (Kasahara et al., 2018; Nishimura et al., 2010, 2011), and microbursts from a few keV to hundreds of keV energies (Breneman et al., 2017; Chen et al., 2021; Nakamura et al., 2000). Whistler-mode hiss waves can extend far within the plasmasphere on the day/dusk side (Ripoll et al., 2022) and cause significant long-lasting scattering of electrons (Ma et al., 2021; Reeves et al., 2016; Ripoll et al., 2016, 2017, 2019). EMIC waves typically occur during geomagnetic storms or substorms (Fraser et al., 2010), as well as during dayside magnetic compressions (Anderson & Hamilton, 1993; Usanova et al., 2012). They are known to be more effective in precipitating relativistic electrons compared to

OIN ET AL. 1 of 10

whistler-mode waves (Angelopoulos et al., 2023; Qin et al., 2018, 2020; Summers & Thorne, 2003; Zhang et al., 2021). Finally, CSS occurs when the particle gyroradius approaches the curvature radius of the magnetic field line as it crosses the plasma sheet (Imhof et al., 1991). In the stretched magnetotail, the curvature radius becomes smaller and can scatter electrons (10 s keV to  $\sim$ MeV) leading to isotropic pitch angle distributions at  $L > \sim 5-6$  at low-Earth-orbit (LEO) (e.g., Capannolo et al., 2022; Wilkins et al., 2023).

While the global distribution of >30 keV electron precipitating flux has been studied using POES data (Lam et al., 2010), these measurements suffer from contamination by ions and penetrating particles (Selesnick et al., 2020; Yando et al., 2011). Although efforts to remove the proton contamination have been made (Peck et al., 2015; Pettit et al., 2021), the correction methods exhibit limited effectiveness when proton contamination is severe (Capannolo et al., 2019). Moreover, POES detects electrons in only two directions, with a narrow field-of-view thus capturing only a small fraction of the loss cone. The occurrence rate of relativistic electron precipitation (REP) (Blum et al., 2015; Carson et al., 2012; Comess et al., 2013; Gasque et al., 2021; Yahnin et al., 2016), as well as the hardness of the electron precipitation flux spectrum has been extensively investigated (Comess et al., 2013; Shekhar et al., 2018; Smith et al., 2016). However, no research has been conducted on the spectrum of the precipitation ratio, determined by the ratio of precipitating to locally trapped flux. Furthermore, the global distribution of the backscattering electrons (e.g., Marshall & Bortnik, 2018; Selesnick et al., 2004) has not been thoroughly analyzed yet. This analysis is crucial not only for understanding atmospheric energy deposition, but also because backscattered electrons may contribute to the electron precipitation in the conjugate hemisphere. This, in turn, further complicates the quantification of precipitation rate (Mourenas et al., 2021).

We address these questions by using electron measurements from the Electron Losses and Fields INvestigation (ELFIN) CubeSat mission (Angelopoulos et al., 2020), which provides unprecedented resolution in both pitch-angle and energy at LEO, enabling us to study the distribution of the precipitation ratio and its energy spectrum. Specifically, we analyze the global distribution of both the precipitating flux and the precipitation ratio to evaluate the differences in their distribution. In addition, we analyze the full energy spectrum of the electron precipitation rate, from which we can infer the underlying precipitation drivers.

# 2. ELFIN Data Analysis

#### 2.1. Instrumentation

The ELFIN mission (Angelopoulos et al., 2020), which was launched in September 2018, consists of two identical CubeSats (ELFIN-A, B) orbiting on a polar orbit ( $\sim$ 93° inclination), with an altitude of  $\sim$ 450 km, an orbital period of  $\sim$ 90 min, and a spin period of  $\sim$ 3 s. The orbital precession rate is about 0.5° per day, indicating that it takes about  $\sim$ 1 year to span all MLTs. The energetic particle detector for electrons (EPDE) can measure electrons over 0.05–5 MeV in 16 energy channels with an energy resolution of  $\Delta E/E < 40\%$ . EPDE maintains a low background with a signal-to-noise ratio of 100:1. It has been designed with dense shielding and coincidence logic to minimize side penetration and effectively eliminate proton contamination. The spin axis of each satellite is maintained perpendicular to the orbital plane, providing a full pitch-angle resolution of electrons twice per spin. The measurements in each spin are subdivided into 16 bins, providing a pitch angle resolution of  $\sim$ 22.5°.

# 2.2. Energetic Electron Precipitation Observed by ELFIN

Figure 1 shows two examples of ELFIN electron measurements, each lasting for 3 min. The locally trapped (Figures 1a and 1h), downward-going (precipitating, Figures 1b and 1i) and upward-going (backscattered, Figures 1d and 1k) electron energy fluxes are averaged differential energy fluxes, which are normalized by solid angles. To better quantify the precipitating and the backscattered level, we examine precipitation ratio, determined by the ratio of averaged precipitating energy flux to averaged trapped energy flux in Figures 1c and 1j (Angelopoulos et al., 2023) and the backscattered ratio (ratio of backscattered to trapped flux) in Figures 1e and 1l. When calculating the ratios, we remove the data with low trapped electron count which leads to unphysically high ratios, by requiring a maximum percentage error of 50%. The precipitation ratio is close to the backscattered ratio during weak precipitation. During the time interval marked with an orange bar (above panel d), the precipitation primarily occurs above 200 keV, and the precipitation ratio increases with energy. This is a typical signature driven by EMIC waves, which is known to be most efficient at high energies above a few hundred keV (Angelopoulos et al., 2023; Capannolo et al., 2023). For the second interval (purple bar above panel d),

OIN ET AL. 2 of 10

19448007, 2024, 10, Downloaded from https://agupubs.onlinelibrary.wiley.com/doi/10.1029/2023GL105134 by Boston University. Wiley Online Library on [30/05/2024]. See the Terms

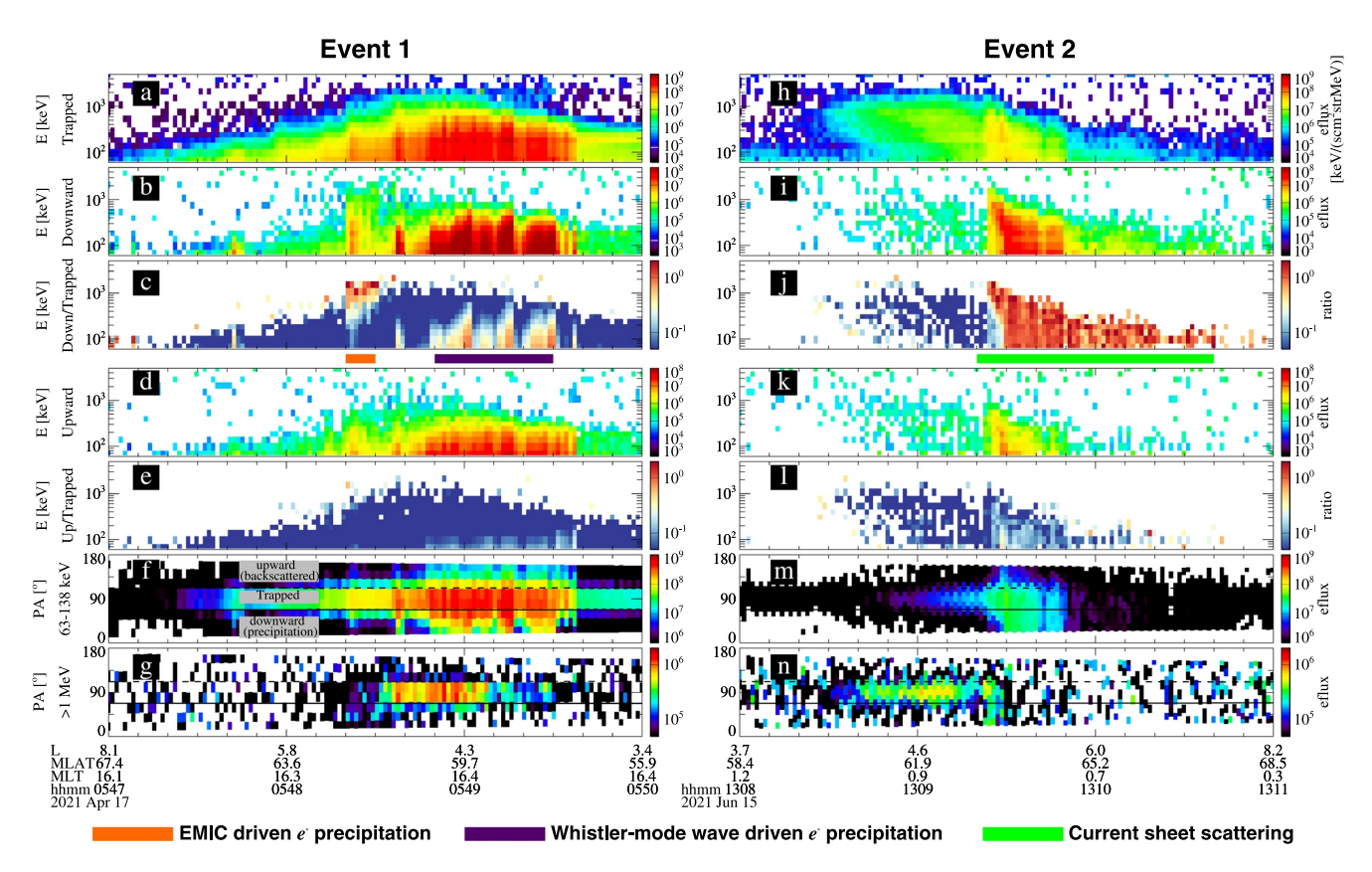


**Figure 1.** Examples of electron precipitation likely driven by electromagnetic ion cyclotron (orange bar between panel c and d), whistler-mode waves (purple bar) and current sheet scattering (green bar). (a, h) Trapped energy flux (averaged energy flux between the loss cone and anti-loss cone); (b, i) downward-going or precipitating energy flux (averaged energy flux inside the bounce loss cone); (c, j) downward (precipitation) ratio; (d, k) upward-going electron (mostly electrons backscattered by the atmosphere at Electron Losses and Fields INvestigation energy) energy flux; (e, l) upward (backscattered) ratio; pitch angle distribution of electron energy fluxes at (f, m) 63–138 keV, and (g, n) >1 MeV. The solid and dashed black lines in panels (f, g, m, n) represent local loss cone and anti-loss cone angles, respectively. The local loss cone is determined by comparing the local magnetic field magnitude to the field magnitude at 100-km foot point in the nearest hemisphere. This differs from the typical definition, which compares it to the minimum field in either the south or north direction at foot points (e.g., Selesnick et al., 2019).

the precipitation only occurs below  $\sim$ 400 keV and the precipitation ratio decreases with increasing energy. This suggests that the precipitation dominates at low energies and could potentially be driven by whistler-mode waves. We computed the plasmapause location, which is at  $L \sim 4.2 \pm 0.5$  (AE  $\sim 500$  nT) (Ripoll et al., 2022). The precipitation occurred over  $L \sim 3.5$ –5, right in the plasmapause transition region, where both whistler-mode chorus and hiss can exist without clear discrimination. For the third time interval (green bar above panel k), the precipitation ratio is close to  $\sim$ 1 (isotropic distribution) with an energy dispersion in L shell. This is typically driven by CSS (e.g., Imhof et al., 1991; Sergeev & Tsyganenko, 1982; Wilkins et al., 2023). Two additional examples of CSS-driven precipitation on the dawnside and duskside are shown in Figure S2 in Supporting Information S1. Note that the measurements of trapped and precipitating flux are not strictly simultaneous (within  $\sim$ 1.5 s), and the times with precipitation ratio >1 might be related to extremely fast electron precipitation through non-linear Landau trapping by oblique whistler mode waves (Zhang et al., 2022) or due to aliasing. The backscattered ratio also increases during the second and third time intervals, while not increasing as the energy increases. This might be because the high-energy electrons are not as efficiently scattered back by the atmosphere as the low-energy electrons (Selesnick et al., 2004).

# 3. Statistical Results

To statistically evaluate the global distribution of electron precipitation at 60 keV and  $\sim$ 1 MeV, as well as the energy spectrum of the precipitation ratio, we use ELFIN measurements of energetic electrons (1.5 s half-spin data) from March 2020 through October 2022. We sorted the data by various geomagnetic activity levels, which were categorized by AE index, and organized the data in bins with a size of  $1 L \times 2 h$  MLT over 3 < L < 10. The

OIN ET AL. 3 of 10

19448007, 2024, 10, Downloaded from https://agupubs.onlinelibrary.wiley.com/doi/10.1029/2023GL/105134 by Boston University, Wiley Online Library on [30/05/2024]. See the Terms and Conditions (https://onlinelibrary.wiley

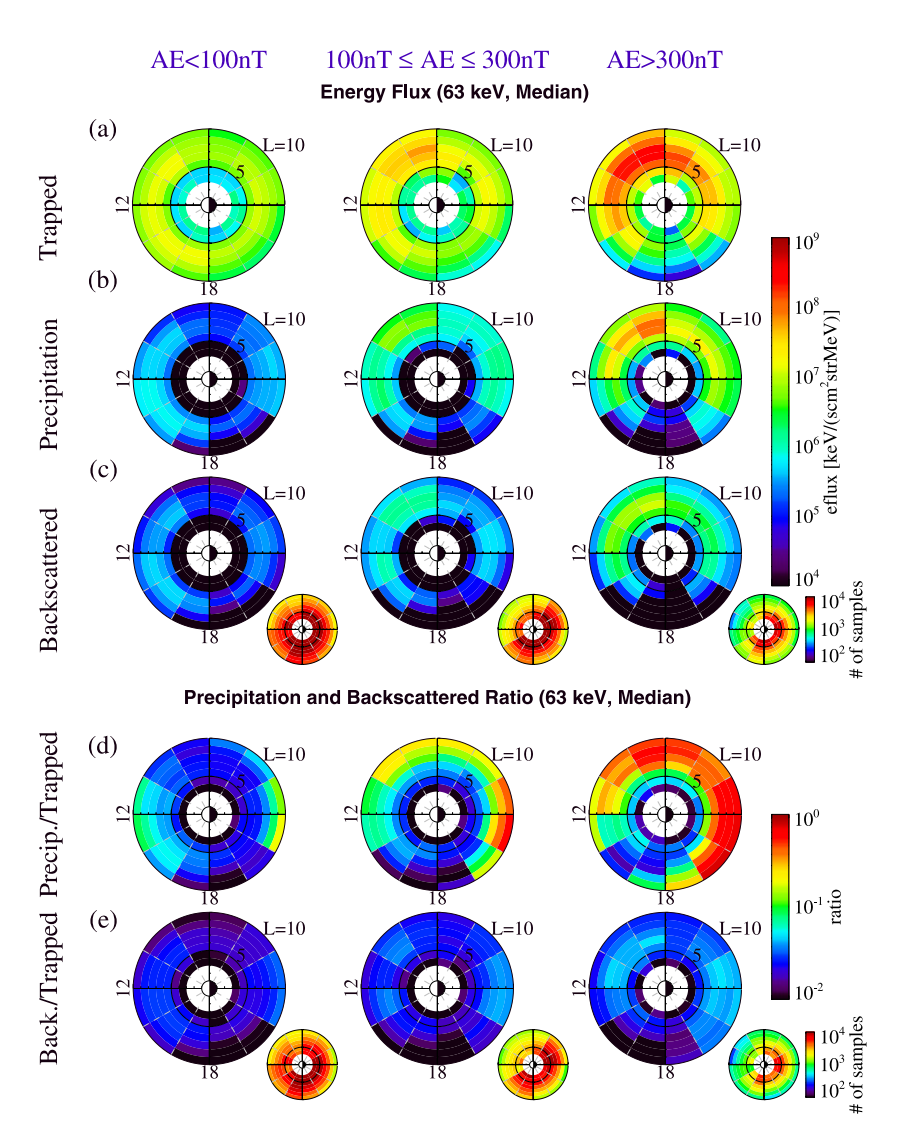


Figure 2. Global distribution of trapped, precipitating and backscattered electrons at 63 keV energy observed at L shells between 3 and 10 categorized by AE index. (a) Median trapped energy flux; (b) median precipitating energy flux; (c) median backscattered energy flux; (d) median value of precipitation ratio and (e) the median value of backscattered ratio. The larger plots show the energy flux (a–c) and the ratio (d–e). The smaller plots show the corresponding number of samples. The total number of samples for panels (a)–(c) is 3,073,342, corresponding to  $\sim$ 1,280 hr, and the total number of samples for panels (d)–(e) is 1,018,998, corresponding to  $\sim$ 424 hr.

L shells are calculated from the T89 magnetic field model (Tsyganenko, 1989). We excluded bins less than 120 samples (3 min, each sample represents measurement from a single half-spin), and data during solar energetic particle events.

# 3.1. Global Distribution of 63 keV Electron Precipitation at LEO

Figures 2a and 2b show the median value of the energy flux in the global L-MLT coordinates for 63 keV electrons, along with the number of samples per bin shown in the smaller plots at the bottom. Figures 2a and 2b indicate that both the trapped and precipitating energy fluxes at 63 keV from midnight to noon (with a peak near dawn) depend on AE, and have much stronger intensity during higher geomagnetic activity. On the duskside (15 hr < MLT < 21 hr), the trapped energy flux decreases with increasing AE index. The distribution of the trapped and precipitating electron energy flux measured by ELFIN is roughly consistent with the POES measurements (Lam et al., 2010; Meredith et al., 2016) during active conditions, both peak around dawn to noon sector. Pitch angle scattering of chorus waves from midnight to noon (Li et al., 2011) can move electrons toward the loss

OIN ET AL. 4 of 10

cone, leading to higher trapped electron flux observed in the dawn sector than the midnight at LEO. During weak geomagnetic conditions, it shows that electron precipitation is observed on the dayside from 08 to 18 hr in MLT at L > 6, isolated from the nightside electron precipitation (22–04 hr MLT) (Figure 2b, left). The dayside electron precipitation is overall similar to POES observations (Lam et al., 2010) and consistent with the distribution of dayside chorus waves during quiet times (Li et al., 2009). Figure 2c shows that the backscattered electron energy flux also increases with enhanced geomagnetic activity. During weak precipitation, the backscattered energy flux is comparable to precipitation energy flux. However, in the region with intense precipitation, only 10%–20% precipitating electrons are backscattered, probably because as the precipitation ratio increases, more electrons are deep in the loss cone and tend to be backscattered less.

Figure 2d shows that the precipitation ratio depends strongly on AE from midnight through dawn to noon. Interestingly, the highest precipitation ratio occurs near midnight, despite the highest energy flux being near the dawn sector. In addition, the precipitation ratio increases as L shell increases. The 63 keV electrons over 6 < L < 10 can be precipitated by both chorus waves and CSS. However, as the nightside chorus waves are located mostly within  $L \sim 8$  (Li et al., 2011; Meredith et al., 2012), the precipitation over 8 < L < 10 is likely driven by CSS. Furthermore, the region of high precipitation ratio moves closer to Earth as the geomagnetic activity increases, which is consistent with the preferential region of chorus generation (Li et al., 2011; Meredith et al., 2012) and the more stretched magnetic field lines during active times. It is also consistent with the trend of dropouts moving toward lower L-shells as activity increases (Pierrard et al., 2020). Electron precipitation distribution also varies with longitude, due to the formation of a drift loss cone associated with the South Atlantic Anomaly. However, this longitudinal dependence normally decreases with higher diffusion rates (Selesnick et al., 2020). Thus, the region with high precipitation ratios primarily reflects the L-MLT effect driven by the underlying scattering mechanisms, rather than SAA-related longitude variation. Moreover, since not all MLTs are covered in the same mission time period, the MLT distributions can be biased by the occurrence of storm activity over the course of the mission and by the solar cycle.

#### 3.2. Global Distribution of 1 MeV Electron Precipitation at LEO

The 75th percentile of the statistical distribution of 1 MeV electrons is presented in Figure 3 (instead of the median values) to highlight the potential precipitation features more clearly. Figure 3a indicates that trapped MeV electrons are mostly confined within  $L \sim 8$ , peaking at  $L \sim 4$ –6. The trapped fluxes of 1 MeV electrons are essentially independent of MLT, due to their shorter gradient-curvature drift time. Both the trapped flux (Figure 3a) and precipitating flux (Figure 3b) tend to increase during higher AE, while the backscattered energy flux (Figure 3c) is less dependent on geomagnetic activity. This result could be influenced by the low count rates of backscattered electrons in the higher energy bins. It is noteworthy that due to ELFIN's low altitude, MeV electrons are less frequently detected compared to other MeV electron measurements at LEO, such as the ESA Proba V satellite at ~800 km (Pierrard et al., 2020, 2021) or CARMEN missions at ~1,336 km (Ginisty et al., 2023a, 2023b).

MeV electron precipitation ratio increases with increasing AE index and remains higher on the nightside than on the dayside at L > 6 (Figure 3d). Unlike the precipitating flux, which peaks over 4 < L < 6, the precipitation ratio peaks over 6 < L < 9. This suggests that although MeV precipitation events occur less frequently at 6 < L < 9, the precipitation efficiency can be higher. Interestingly, the precipitation ratio noticeably increases near the dusk sector during AE > 300 nT, which may be related to the enhanced precipitation due to EMIC waves (Capannolo et al., 2023), though a further investigation is required to verify this correlation. Around midnight, MeV electrons can be precipitated by CSS, EMIC or other waves (e.g., whistler-mode chorus or hiss). Recent ELFIN statistics from >800 CSS events (Wilkins et al., 2023) confirm their peak occurrence at around 22 MLT and extend with >50% probability over 20–03 MLT, with >80% of events occurring at  $L \sim 6$ –9. Capannolo et al. (2022) showed that EMIC wave-driven REP events occur mainly at L < 7 around midnight. Therefore, the peak precipitation ratio near midnight at L > 7 in our study is likely driven by CSS or other waves. Little MeV precipitation is observed on the dayside, even though this region is favorable for EMIC wave generation (Saikin et al., 2015; Usanova et al., 2012). One potential reason is the relatively low ratio between the plasma frequency and electron cyclotron frequency in this region, which leads to the higher resonance energy, typically above several MeV. The backscattered ratio of MeV electrons is consistently low during all geomagnetic conditions (Figure 3e). This is because the higher energy electrons penetrate to lower altitudes in the atmosphere and thus have a lower chance of being backscattered (Marshall & Bortnik, 2018; Selesnick et al., 2004).

OIN ET AL. 5 of 10

1944/8007, 2024, 10, Downloaded from https://agupubs.onlinelibrary.wiley.com/doi/10.1029/2023GL105134 by Boston University, Wiley Online Library on [30/05/2024]. See the Terms and Conditions (https://onlinelibrary.wiley.com/terms-and-conditions)

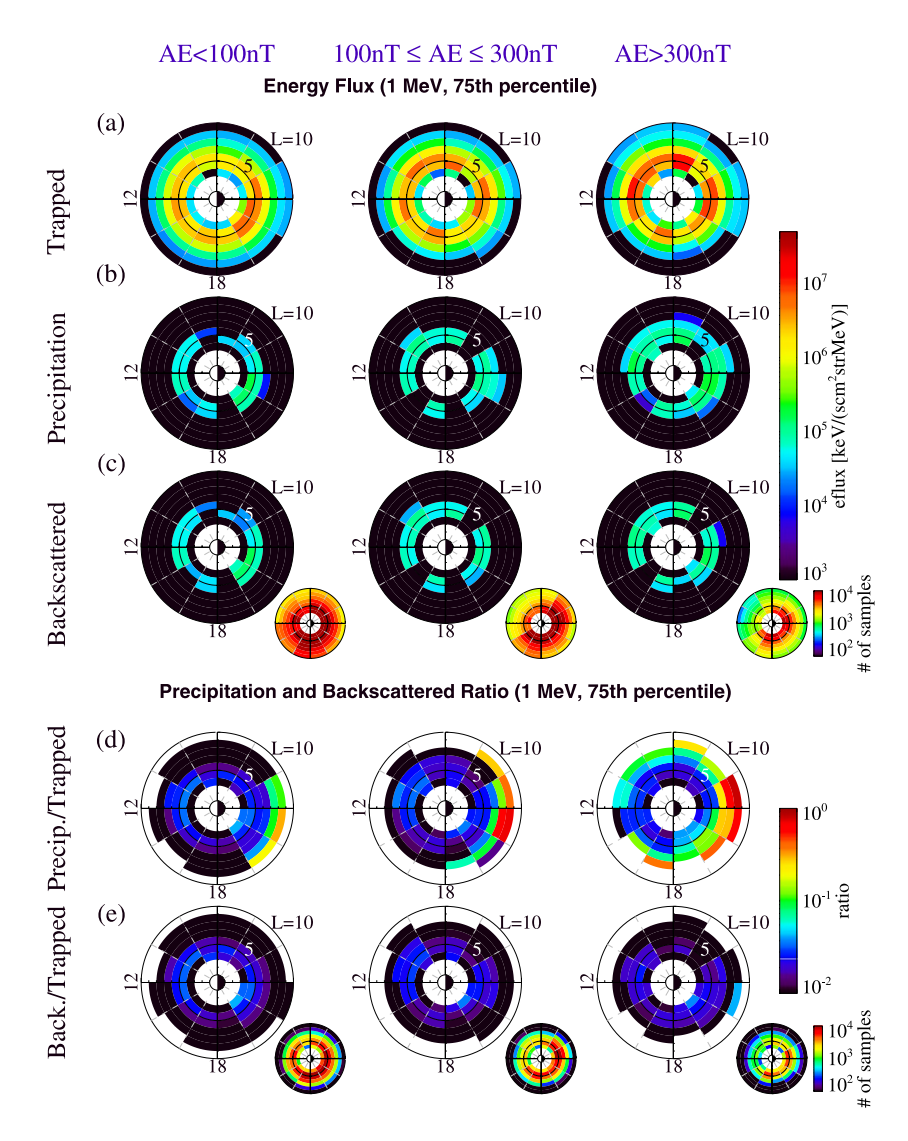


Figure 3. Same as Figure 2, except for 75th percentile value for 1 MeV electrons. Total number of samples for panels (a)–(c) is 3,073,342, corresponding to  $\sim$ 1,280 hr, and total number of samples for panels (d)–(e) is 516,509, corresponding to  $\sim$ 215 hr.

#### 3.3. Energy Spectrum of Energetic Electron Precipitation Ratio at LEO

To better understand the scattering process, we further analyze the energy spectrum of the precipitation ratios at various L shells in four specific MLT ranges: dawnside (03–09 MLT), noon (09–15 MLT), duskside (15–21 MLT), and midnight (21–03 MLT). The statistical dependence on AE index is further discussed in Figures S2–S4 and Text S2 in Supporting Information S1.

The median precipitation ratio (Figure 4a–4d) steeply decreases with increasing energy from 60 keV to  $\sim$ 200–300 keV, with a precipitation ratio of  $\sim$ 0.1 at 60 keV and only 0.01 at 200–300 keV. This feature is consistent with chorus-driven precipitation (e.g., Ma et al., 2020; Ni et al., 2011; Shen et al., 2023), indicating significant contributions from both dayside and nightside chorus waves. In contrast, for energies above  $\sim$ 200–300 keV, the median precipitation ratio quickly drops down to 0 for all MLT sectors at L > 6. This suggests that the statistical data are dominated by the times with no precipitation, with higher energy electron precipitation occurring less frequently compared to lower energies.

Since statistical results may be dominated by the times with no precipitation, various quantiles, including 75% (Figures 4e–4h), 90% (Figures 4i–4l), and mean values (Figures 4m–4p), are examined to enable a more effective identification of the characteristics associated with periods of precipitation occurrence. In contrast, the 90th

OIN ET AL. 6 of 10

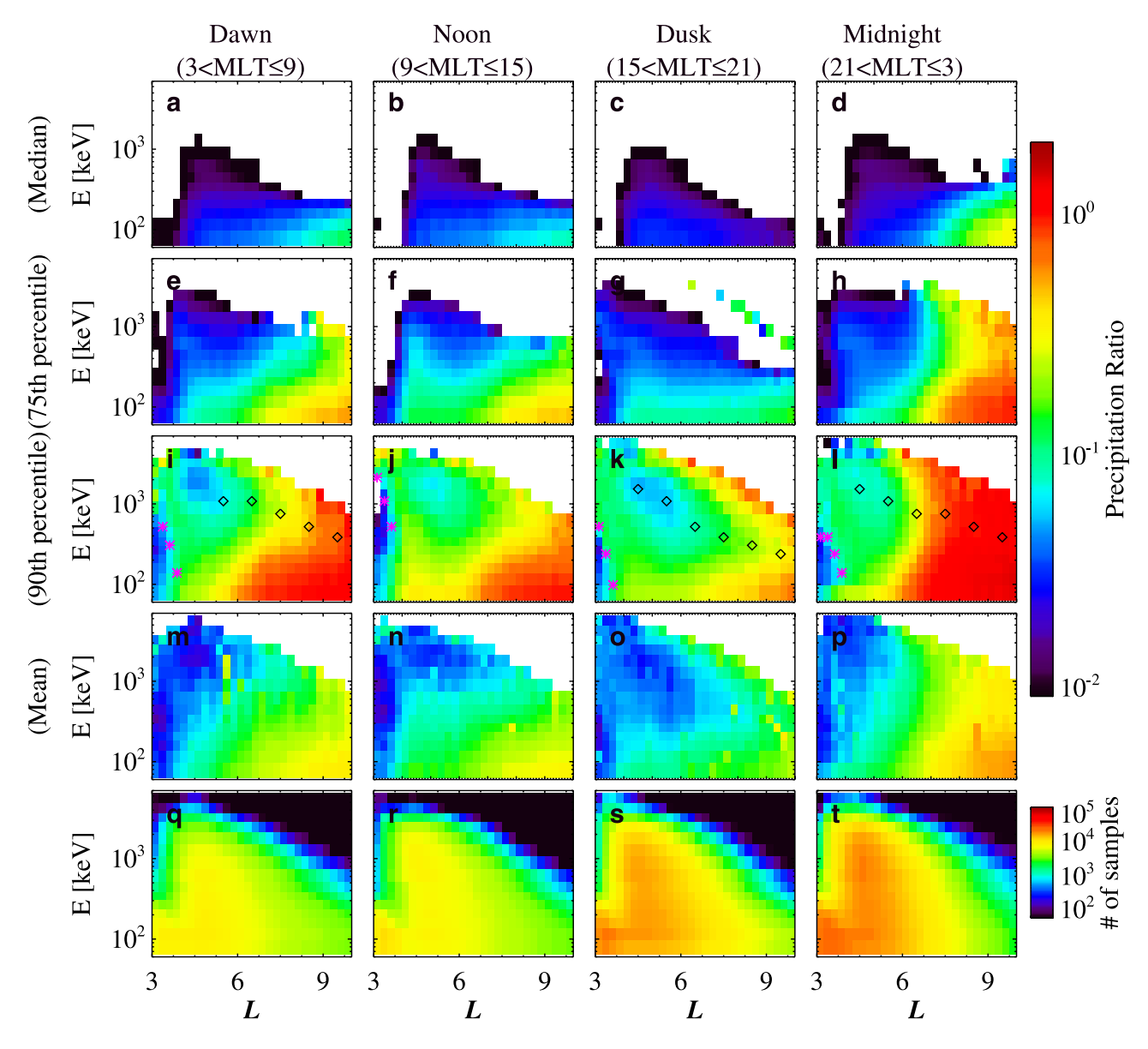


**Figure 4.** Energy spectrum of the statistical median (a–d), 75th percentile (e–h), 90th percentile (i–l) and mean (m–p) values of the precipitation ratio on the dawnside, noon, duskside and midnight. Panels (q–t) represent the number of samples. The black diamonds and magenta asterisks in panels (i–l) represent the reversal energy points where the precipitation ratios begin to increase as energy increases. The line plot of this figure is shown in Figures S5 in Supporting Information S1.

percentile (75th percentile shown as a transition) and mean precipitation ratio decrease with energy at low energies, then increase again as energy increases at  $L > \sim 6$  on the dawnside, duskside and midnight. Interestingly, the reversal points (black diamonds, which are estimated at the points where precipitation ratios begin to increase as energy increases) show energy dispersion in L shell, with higher energies at lower L shells. This feature is consistent with precipitation due to CSS. In the slot region at 3 < L < 4, the energy range with maximum precipitation ratio (above magenta stars) aligns with resonant energies driven by hiss-driven precipitation, which also shows dispersion along L shells, with higher resonant energy at lower L shells, as shown in Figure 2 in both Ripoll et al. (2019) and Ma et al. (2016). Notably, the hardest spectrum of the precipitation ratio (with energy above the black diamonds) is observed on the duskside. This feature is consistent with that shown in Comess et al. (2013) where the hardest spectrum of precipitation is found over 15–02 hr in MLT using SAMPEX data. It is likely due to REP driven by EMIC waves, which preferentially occurs near the dusk sector (e.g., Capannolo et al., 2023; Millan & Thorne, 2007; Summers & Thorne, 2003).

OIN ET AL. 7 of 10

# 4. Summary and Conclusions

We present the global distribution and energy spectrum of electron measurements at LEO during different geomagnetic conditions using ELFIN data. Our survey focuses on 60 keV and 1 MeV electrons and provides accurate measurements of trapped, precipitating, and backscattered electron fluxes. Moreover, our study shows statistical results from the full energy spectrum of the precipitation ratio. We summarize the key findings as follows.

- 1. The trapped, precipitating, and backscattered electron flux at  $\sim$ 63 keV and their associated precipitation and backscattered ratios tend to increase with increasing geomagnetic activity. The distribution of the precipitation ratio of  $\sim$ 63 keV electrons peaks at high L shells (L>6) at midnight during active conditions, in contrast to the distribution of precipitating energy flux, which peaks from the dawn to noon sector. This distribution of precipitation ratio at  $\sim$ 63 keV differs from that of chorus waves, the intensities of which are mainly confined to L<8 on the nightside (Li et al., 2011). This suggests that the  $\sim$ 63 keV electron precipitation is likely due to a combined effect of both chorus waves and CSS, with CSS being mostly responsible for the high precipitation ratios at L>8. However, the relative contribution of these two mechanisms at other locations requires further quantification. During weak precipitation, the backscattered energy flux is comparable to or slightly lower than precipitation energy flux. However, during intense precipitation, only 10%–20% precipitating electrons are backscattered.
- 2. During weak geomagnetic conditions,  $\sim$ 63 keV electron precipitation is predominantly observed on the dayside at L > 6, which is consistent with the higher occurrence of quiet-time chorus waves on the dayside than the nightside (Li et al., 2009).
- 3. The 1 MeV trapped electron distributions are mostly confined to L < 8 and almost independent of MLT. Both the trapped and precipitating electron fluxes increase with increasing geomagnetic activity, while backscattered fluxes are almost independent of geomagnetic activity. The precipitation ratio is higher on the night-side than on the dayside, which is likely due to the combined effect of EMIC waves, CSS, or pitch angle scattering by other waves. Interestingly, the precipitation ratio increases near the dusk sector during active geomagnetic conditions, which may be related to the enhanced MeV electron precipitation driven by EMIC waves. Moreover, little weak MeV precipitation is observed on the dayside at high L shells, even though this region is favorable for EMIC wave generation (Usanova et al., 2012).</p>
- 4. The energy spectrum of the precipitation ratio shows that MeV electron precipitation occurs much less frequently than electron precipitation with energies below ~1 MeV. Interestingly, the energy spectrum of the precipitation ratio shows reversal points indicating energy dispersion in L shells in both the slot region at 3 < L < 4 and L > ~6, a feature consistent with the precipitation driven by hiss waves and CSS, respectively. Notably, the hardest spectrum of the precipitation ratio (with energy above the black diamonds in Figure 4) is observed on the duskside, likely driven by EMIC waves.

The high pitch angle and energy resolution, together with the high-quality measurements with minimal background and contamination from ELFIN, contribute to accurately quantifying electron precipitation in a broad region of the Earth's magnetosphere and provide insights into the underlying physical mechanisms of precipitating electrons from the magnetosphere into the upper atmosphere.

## **Data Availability Statement**

ELFIN EPDE data are used for electron energy flux measurement (Angelopoulos et al., 2018). Data used for the statistical figures are available from Qin et al. (2023).

#### References

Anderson, B. J., & Hamilton, D. C. (1993). Electromagnetic ion cyclotron waves stimulated by modest magnetospheric compressions. *Journal of Geophysical Research*, 98(A7), 11369–11382. https://doi.org/10.1029/93JA00605

Angelopoulos, V., Tsai, E., Bingley, L., Shaffer, C., Turner, D. L., Runov, A., et al. (2018). ELFIN/EPDE [Dataset]. UCLA. Retrieved from https://themis-data.igpp.ucla.edu/elfindata/

Angelopoulos, V., Tsai, E., Bingley, L., Shaffer, C., Turner, D. L., Runov, A., et al. (2020). The ELFIN mission. Space Science Reviews, 216(5), 103. https://doi.org/10.1007/s11214-020-00721-7

Angelopoulos, V., Zhang, X. J., Artemyev, A. V., Mourenas, D., Tsai, E., Wilkins, C., et al. (2023). Energetic electron precipitation driven by electromagnetic ion cyclotron waves from ELFIN's low altitude perspective. *Space Science Reviews*, 219(5), 37. https://doi.org/10.1007/s11214-023-00984-w

#### Acknowledgments

MQ, WL, XS, QM, and LC would like to acknowledge NASA grants of 80NSSC20K0698, 80NSSC21K1312, 80NSSC20K0196, NSF grants of AGS-1847818, AGS-2019950, AGS-2225445, and AGS-2247774. We acknowledge NASA award NNX14AN68G and NSF awards AGS-1242918, AGS-2019950, and AGS-2247774, the ELFIN team for use of EPD data.

OIN ET AL. 8 of 10

- Blum, L., Li, X., & Denton, M. (2015). Rapid MeV electron precipitation as observed by SAMPEX/HILT during high-speed stream-driven storms. *Journal of Geophysical Research: Space Physics*, 120(5), 3783–3794. https://doi.org/10.1002/2014JA020633
- Breneman, A. W., Crew, A., Sample, J., Klumpar, D., Johnson, A., Agapitov, O., et al. (2017). Observations directly linking relativistic electron microbursts to whistler mode chorus: Van Allen Probes and FIREBIRD II. Geophysical Research Letters, 44(22), 11265–11272. https://doi.org/10.1002/2017GL075001
- Capannolo, L., Li, W., Ma, Q., Qin, M., Shen, X.-C., Angelopoulos, V., et al. (2023). Electron precipitation observed by ELFIN using proton precipitation as a proxy for electromagnetic ion cyclotron (EMIC) waves. *Geophysical Research Letters*, 50(21), e2023GL103519. https://doi.org/10.1029/2023GL103519
- Capannolo, L., Li, W., Ma, Q., Shen, X.-C., Zhang, X.-J., Redmon, R. J., et al. (2019). Energetic electron precipitation: Multievent analysis of its spatial extent during EMIC wave activity. *Journal of Geophysical Research: Space Physics*, 124(4), 2466–2483. https://doi.org/10.1029/2018JA026291
- Capannolo, L., Li, W., Millan, R., Smith, D., Sivadas, N., Sample, J., & Shekhar, S. (2022). Relativistic electron precipitation near midnight: Drivers, distribution, and properties. *Journal of Geophysical Research: Space Physics*, 127(1), e2021JA030111, https://doi.org/10.1029/2021JA030111
- Carson, B. R., Rodger, C. J., & Clilverd, M. A. (2012). POES satellite observations of EMIC-wave driven relativistic electron precipitation during 1998–2010. *Journal of Geophysical Research*, 118(1), 232–243. https://doi.org/10.1029/2012JA017998
- Chen, L., Zhang, X.-J., Artemyev, A., Zheng, L., Xia, Z., Breneman, A. W., & Horne, R. B. (2021). Electron microbursts induced by nonducted chorus waves. Frontiers in Astronomy and Space Sciences, 8, 745927. https://doi.org/10.3389/fspas.2021.745927
- Comess, M. D., Smith, D. M., Selesnick, R. S., Millan, R. M., & Sample, J. G. (2013). Duskside relativistic electron precipitation as measured by SAMPEX: A statistical survey. *Journal of Geophysical Research: Space Physics*, 118(8), 5050–5058. https://doi.org/10.1002/jgra.50481
- Fraser, B. J., Grew, R. S., Morley, S. K., Green, J. C., Singer, H. J., Loto'aniu, T. M., & Thomsen, M. F. (2010). Storm time observations of electromagnetic ion cyclotron waves at geosynchronous orbit: GOES results. *Journal of Geophysical Research*, 115(A5), A05208. https://doi.org/10.1029/2009JA014516
- Gasque, L. C., Millan, R. M., & Shekhar, S. (2021). Statistically determining the spatial extent of relativistic electron precipitation events using 2-s polar-orbiting satellite data. *Journal of Geophysical Research: Space Physics*, 126(4), e2020JA028675. https://doi.org/10.1029/2020JA028675
- Ginisty, F., Wrobel, F., Ecoffet, R., Balcon, N., Mekki, J., Ruffenach, M., et al. (2023a). Comparison of relativistic electron flux at low Earth orbit (LEO) and electric orbit raising (EOR) from the CARMEN missions. Advances in Space Research, 71(10), 4401–4409. https://doi. org/10.1016/j.asr.2023.01.002
- Ginisty, F., Wrobel, F., Ecoffet, R., Standarovski, D., Mekki, J., Ruffe- nach, M., et al. (2023b). CARMEN 2 and 3 LEO electron flux measurements linear projection onto RBSP elliptical orbit. IEEE Transactions on Nuclear Science, 70(8), 1564–1571. https://doi.org/10.1109/TNS.2023.3260904
- Imhof, W. L., Voss, H. D., Mobilia, J., Datlowe, D. W., & Gaines, E. E. (1991). The precipitation of relativistic electrons near the trapping boundary. *Journal of Geophysical Research*, 96(A4), 5619–5629. https://doi.org/10.1029/90JA02343
- Kasahara, S., Miyoshi, Y., Yokota, S., Mitani, T., Kasahara, Y., Matsuda, S., et al. (2018). Pulsating aurora from electron scattering by chorus waves. *Nature*, 554(7692), 337–340. https://doi.org/10.1038/nature25505
- Lam, M. M., Horne, R. B., Meredith, N. P., Glauert, S. A., Moffat-Griffin, T., & Green, J. C. (2010). Origin of energetic electron precipitation >30 keV into the atmosphere. *Journal of Geophysical Research*, 115(A4), A00F08. https://doi.org/10.1029/2009JA014619
- Li, W., Bortnik, J., Thorne, R. M., & Angelopoulos, V. (2011). Global distribution of wave amplitudes and wave normal angles of chorus waves using THEMIS wave observations. *Journal of Geophysical Research*, 116(A12), A12205. https://doi.org/10.1029/2011JA017035
- Li, W., & Hudson, M. K. (2019). Earth's Van allen radiation belts: From discovery to the Van Allen probes era. Journal of Geophysical Research: Space Physics, 124(11), 8319–8351. https://doi.org/10.1029/2018JA025940
- Li, W., Thorne, R. M., Angelopoulos, V., Bortnik, J., Cully, C. M., Ni, B., et al. (2009). Global distribution of whistler-mode chorus waves observed on the THEMIS spacecraft. Geophysical Research Letters, 36(9), L09104. https://doi.org/10.1029/2009GL037595
- Ma, Q., Connor, H. K., Zhang, X.-J., Li, W., Shen, X.-C., Gillespie, D., et al. (2020). Global survey of plasma sheet electron precipitation due to whistler mode chorus waves in Earth's magnetosphere. Geophysical Research Letters, 47(15), e2020GL088798. https://doi. org/10.1029/2020GL088798
- Ma, Q., Li, W., Thorne, R. M., Bortnik, J., Reeves, G. D., Kletzing, C. A., et al. (2016). Characteristic energy range of electron scattering due to plasmaspheric hiss. *Journal of Geophysical Research: Space Physics*, 121(12), 11737–11749. https://doi.org/10.1002/2016JA023311
- Ma, Q., Li, W., Zhang, X.-J., Bortnik, J., Shen, X.-C., Connor, H. K., et al. (2021). Global survey of electron precipitation due to hiss waves in the Earth's plasmasphere and plumes. *Journal of Geophysical Research: Space Physics*, 126(8), e2021JA029644. https://doi.org/10.1029/2021JA029644
- Marshall, R. A., & Bortnik, J. (2018). Pitch angle dependence of energetic electron precipitation: Energy deposition, backscatter, and the bounce loss cone. *Journal of Geophysical Research*, 123(3), 2412–2423. https://doi.org/10.1002/2017JA024873
- Meredith, N. P., Horne, R. B., Isles, J. D., & Green, J. C. (2016). Extreme energetic electron fluxes in low Earth orbit: Analysis of POES *E* > 30, *E* > 100, and *E* > 300 keV electrons. *Space Weather*, *14*(2), 136–150. https://doi.org/10.1002/2015SW001348
- Meredith, N. P., Horne, R. B., Sicard-Piet, A., Boscher, D., Yearby, K. H., Li, W., & Thorne, R. M. (2012). Global model of lower band and upper band chorus from multiple satellite observations. *Journal of Geophysical Research*, 117(A10), A10225. https://doi.org/10.1029/2012JA017978
- Millan, R. M., & Thorne, R. M. (2007). Review of radiation belt relativistic electron losses. *Journal of Atmospheric and Terrestrial Physics*, 69(3), 362–377. https://doi.org/10.1016/jastp.2006.06.019
- Mourenas, D., Artemyev, A. V., Zhang, X.-J., Angelopoulos, V., Tsai, E., & Wilkins, C. (2021). Electron lifetimes and diffusion rates inferred from ELFIN measurements at low altitude: First results. *Journal of Geophysical Research: Space Physics*, 126(11), e2021JA029757. https://doi.org/10.1029/2021JA029757
- Nakamura, R., Isowa, M., Kamide, Y., Baker, D. N., Blake, J. B., & Looper, M. (2000). SAMPEX observations of precipitation bursts in the outer radiation belt. *Journal of Geophysical Research*, 105(A7), 15875–15885. https://doi.org/10.1029/2000JA900018
- Ni, B., Thorne, R. M., Meredith, N. P., Horne, R. B., & Shprits, Y. Y. (2011). Resonant scattering of plasma sheet electrons leading to diffuse auroral precipitation: 2. Evaluation for whistler mode chorus waves. *Journal of Geophysical Research*, 116(A4), A04219. https://doi.org/10.1029/2010JA016233
- Nishimura, Y., Bortnik, J., Li, W., Thorne, R. M., Chen, L., Lyons, L. R., et al. (2011). Multievent study of the correlation between pulsating aurora and whistler mode chorus emissions. *Journal of Geophysical Research*, 116(A11), A11221. https://doi.org/10.1029/2011JA016876
- Nishimura, Y., Bortnik, J., Li, W., Thorne, R. M., Lyons, L. R., Angelopoulos, V., et al. (2010). Identifying the driver of pulsating aurora. *Science*, 330(6000), 81–84. https://doi.org/10.1126/science.1193186
- Peck, E. D., Randall, C. E., Green, J. C., Rodriguez, J. V., & Rodger, C. J. (2015). POES MEPED differential flux retrievals and electron channel contamination correction. *Journal of Geophysical Research: Space Physics*, 120(6), 4596–4612. https://doi.org/10.1002/2014JA020817

QIN ET AL. 9 of 10

- Pettit, J. M., Randall, C. E., Peck, E. D., & Harvey, V. L. (2021). A new MEPED-based precipitating electron data set. *Journal of Geophysical Research: Space Physics*, 126(12), e2021JA029667. https://doi.org/10.1029/2021JA029667
- Pierrard, V., Botek, E., Ripoll, J.-F., & Cunningham, G. (2020). Electron dropout events and flux enhancements associated with geomagnetic storms observed by PROBAV/energetic particle telescope from 2013 to 2019. *Journal of Geophysical Research: Space Physics*, 125(12), e2020JA028487. https://doi.org/10.1029/2020JA028487
- Pierrard, V., Ripoll, J.-F., Cunningham, G., Botek, E., Santolik, O., Thaller, S., et al. (2021). Observations and simulations of dropout events and flux decays in October 2013: Comparing MEO equatorial with LEO polar orbit. *Journal of Geophysical Research: Space Physics*, 126(6), e2020JA028850. https://doi.org/10.1029/2020JA028850
- Qin, M., Hudson, M., Millan, R., Woodger, L., & Shekhar, S. (2018). Statistical investigation of the efficiency of EMIC waves in precipitating relativistic electrons. *Journal of Geophysical Research: Space Physics*, 123(8), 223–6230. https://doi.org/10.1029/2018JA025419
- Qin, M., Hudson, M., Millan, R., Woodger, L., & Shen, X. (2020). Statistical dependence of EMIC wave scattering on wave and plasma parameters. *Journal of Geophysical Research: Space Physics*, 125(4), e2020JA027772. https://doi.org/10.1029/2020JA027772
- Qin, M., Li, W., Shen, X.-C., Angelopoulos, V., Selesnick, R., Capannolo, L., et al. (2023). Dataset for global survey of electron precipitation observed by ELFIN at low-Earth-orbit [Dataset]. Figshare. Retrieved from https://figshare.com/articles/dataset/Dataset\_global\_survey\_of\_energetic\_electron\_precipitation\_observed\_by\_ELFIN\_at\_LEO/24526123
- Reeves, G. D., Friedel, R. H. W., Larsen, B. A., Skoug, R. M., Funsten, H. O., Claudepierre, S. G., et al. (2016). Energy dependent dynamics of keV to MeV electrons in the inner zone, outer zone, and slot regions. *Journal of Geophysical Research: Space Physics*, 121(1), 397–412. https://doi.org/10.1002/2015JA021569
- Ripoll, J.-F., Claudepierre, S. G., Ukhorskiy, A. Y., Colpitts, C., Li, X., Fennell, J., & Crabtree, C. (2020). Particle dynamics in the earth's radiation belts: Review of current research and open questions. *Journal of Geophysical Research: Space Physics*, 125(5), e2019JA026735. https://doi.org/10.1029/2019JA026735
- Ripoll, J.-F., Loridan, V., Denton, M. H., Cunningham, G., Reeves, G., Santolík, O., et al. (2019). Observations and Fokker-Planck simulations of the L-shell, energy, and pitch angle structure of Earth's electron radiation belts during quiet times. *Journal of Geophysical Research: Space Physics*, 124(2), 1125–1142. https://doi.org/10.1029/2018JA026111
- Ripoll, J.-F., Reeves, G. D., Cunningham, G. S., Loridan, V., Denton, M., Santolík, O., et al. (2016). Reproducing the observed energy-dependent structure of Earth's electron radiation belts during storm recovery with an event-specific diffusion model. Geophysical Research Letters, 43(11), 5616–5625, https://doi.org/10.1002/2016GL068869
- Ripoll, J.-F., Santolík, O., Reeves, G. D., Kurth, W. S., Denton, M. H., Loridan, V., et al. (2017). Effects of whistler mode hiss waves in March 2013. Journal of Geophysical Research: Space Physics, 122(7), 7433–7462. https://doi.org/10.1002/2017JA024139
- Ripoll, J.-F., Thaller, S. A., Hartley, D. P., Cunningham, G. S., Pierrard, V., Kurth, W. S., et al. (2022). Statistics and empirical models of the plasmasphere boundaries from the Van Allen Probes for radiation belt physics. *Geophysical Research Letters*, 49(21), e2022GL101402. https:// doi.org/10.1029/2022GL101402
- Saikin, A. A., Zhang, J.-C., Allen, R. C., Smith, C. W., Kistler, L. M., Spence, H. E., et al. (2015). The occurrence and wave properties of H+-He+-and O+-band EMIC waves observed by the Van Allen Probes. *Journal of Geophysical Research: Space Physics*, 120(9), 7477–7492. https://doi.org/10.1002/2015JA021358
- Selesnick, R. S., Looper, M. D., & Albert, J. M. (2004). Low-altitude distribution of radiation belt electrons. *Journal of Geophysical Research*, 109(A11), A11209. https://doi.org/10.1029/2004JA010611
- Selesnick, R. S., Su, Y.-J., & Sauvaud, J.-A. (2019). Energetic electrons below the inner radiation belt. Journal of Geophysical Research: Space Physics, 124(7), 5421–5440. https://doi.org/10.1029/2019JA026718
- Selesnick, R. S., Tu, W., Yando, K. B., Millan, R. M., & Redmon, R. J. (2020). POES/MEPED angular response functions and the precipitating radiation belt electron flux. *Journal of Geophysical Research: Space Physics*, 125(9), e2020JA028240. https://doi.org/10.1029/2020JA028240
- Sergeev, V. A., & Tsyganenko, N. A. (1982). Energetic particle losses and trapping boundaries as deduced from calculations with a realistic magnetic field model. *Planetary and Space Science*, 30(10), 999–1006. https://doi.org/10.1016/0032-0633(82)90149-0
- Shekhar, S., Millan, R. M., & Hudson, M. K. (2018). A statistical study of spatial variation of relativistic electron precipitation energy spectra with Polar Operational Environmental Satellites. *Journal of Geophysical Research: Space Physics*, 123(5), 3349–3359. https://doi.org/10.1002/2017JA025041
- Shen, X.-C., Li, W., Capannolo, L., Ma, Q., Qin, M., Artemyev, A. V., et al. (2023). Modulation of energetic electron precipitation driven by three types of whistler mode waves. *Geophysical Research Letters*, 50(8), e2022GL101682. https://doi.org/10.1029/2022GL101682
- Smith, D. M., Casavant, E. P., Comess, M. D., Liang, X., Bowers, G. S., Selesnick, R. S., et al. (2016). The causes of the hardest electron precipitation events seen with SAMPEX. *Journal of Geophysical Research: Space Physics*, 121(9), 8600–8613. https://doi.org/10.1002/2016JA022346
- Summers, D., & Thorne, R. (2003). Relativistic electron pitch-angle scattering by electromagnetic ion cyclotron waves during geomagnetic storms. *Journal of Geophysical Research*, 108(A4), 1143. https://doi.org/10.1029/2002JA009489
- Thorne, R. M. (2010). Radiation belt dynamics: The importance of wave-particle interactions. *Geophysical Research Letters*, 37(22), L22107. https://doi.org/10.1029/2010GL044990
- Thorne, R. M., Ni, B., Tao, X., Horne, R. B., & Meredith, N. P. (2010). Scattering by chorus waves as the dominant cause of diffuse auroral precipitation. *Nature*, 467(7318), 943–946. https://doi.org/10.1038/nature09467
- Tsyganenko, N. A. (1989). A solution of the Chapman-Ferraro problem for an ellipsoidal magnetopause. *Planetary and Space Science*, 37(9), 1037–1046. https://doi.org/10.1016/0032-0633(89)90076-7
- Usanova, M. E., Mann, I. R., Bortnik, J., Shao, L., & Angelopoulos, V. (2012). THEMIS observations of electromagnetic ion cyclotron wave occurrence: Dependence on AE, SYMH, and solar wind dynamic pressure. *Journal of Geophysical Research*, 117(A10), A10218. https://doi. org/10.1029/2012JA018049
- Wilkins, C., Angelopoulos, V., Runov, A., Artemyev, A., Zhang, X.-J., Liu, J., & Tsai, E. (2023). Statistical characteristics of the electron isotropy boundary. *Journal of Geophysical Research: Space Physics*, 128(10), e2023JA031774. https://doi.org/10.1029/2023JA031774
- Yahnin, A. G., Yahnina, T. A., Semenova, N. V., Gvozdevsky, B. B., & Pashin, A. B. (2016). Relativistic electron precipitation as seen by NOAA POES. *Journal of Geophysical Research: Space Physics*, 121(9), 8286–8299. https://doi.org/10.1002/2016JA022765
- Yando, K., Millan, R. M., Green, J. C., & Evans, D. S. (2011). A Monte Carlo simulation of the NOAA POES medium energy proton and electron detector instrument. *Journal of Geophysical Research*. 116(A10), A10231. https://doi.org/10.1029/2011JA016671
- Zhang, X. J., Artemyev, A., Angelopoulos, V., Tsai, E., Wilkins, C., Kasahara, S., et al. (2022). Superfast precipitation of energetic electrons in the radiation belts of the Earth. *Nature Communications*, 13(1), 1611. https://doi.org/10.1038/s41467-022-29291-8
- Zhang, X.-J., Mourenas, D., Shen, X.-C., Qin, M., Artemyev, A. V., Ma, Q., et al. (2021). Dependence of relativistic electron precipitation in the ionosphere on EMIC wave minimum resonant energy at the conjugate equator. *Journal of Geophysical Research*, 126(5), e2021JA029193. https://doi.org/10.1029/2021JA029193

OIN ET AL. 10 of 10